



Finite element analysis of the impact of bone nanostructure on its piezoelectric response

Salil Pai¹ · Jinha Kwon^{1,2} · Bowen Liang³ · Hanna Cho¹ · Soheil Soghrati^{1,4}

Received: 20 January 2021 / Accepted: 22 May 2021 / Published online: 28 June 2021
© The Author(s), under exclusive licence to Springer-Verlag GmbH Germany, part of Springer Nature 2021

Abstract

The piezoelectric response of bone at the submicron scale is analyzed under mechanical loadings using the finite element (FE) method. A new algorithm is presented to virtually reconstruct realistic bone nanostructures, consisting of collagen fibrils embedded in a hydroxyapatite mineral network. This algorithm takes into account potential misalignments between fibrils, as well as the porous structure of the mineral phase. A parallel non-iterative mesh generation algorithm is utilized to create high-fidelity FE models for several representative volume elements (RVEs) of the bone with various fibrils volume fractions and misalignments. The piezoelectric response of each RVE is simulated under three types of loading: the longitudinal compression, lateral compression, and shear. The resulting homogenized stress and electric field in RVEs with aligned fibrils showed a linear variation with the fibrils volume fraction under all loading conditions. For RVEs with misaligned fibrils, although more oscillations were observed in homogenized results, their difference with the results of RVEs with aligned fibrils subject to lateral compression and shear loadings were negligible. However, under longitudinal compression, the electric field associated with RVEs with misaligned fibrils was notably higher than that of RVEs with aligned fibrils for the same volume fraction.

Keywords Bone · Piezoelectric · Nanostructure · Collagen fibrils · Finite element method · Electric potential

1 Introduction

Human bone is composed of ~40% collagen, ~50% mineral, and ~10% of other non-collagenous protein and water (Genin et al. 2009), although this ratio could vary depending on age and health conditions. While these constituents are made of both soft organic and brittle inorganic phases, the bone exhibits remarkable mechanical properties with a high strength and toughness (Reilly et al. 1974; Norman et al. 1995), as well as the ability to repair itself (Taylor et al. 2007). This is made possible due to the hierarchical

architecture of bone (Rho et al. 1998; Fratzl and Weinkamer 2007), ranging from tropocollagen molecules to bundles of collagen fibers at the scale of few microns to osteons at the scale of ~100 μm and finally at the macroscale, where its length can reach up to ~50 cm (Reznikov et al. 2014). Various intrinsic and extrinsic mechanisms at different length scales are responsible for toughening of the bone (Ritchie et al. 2009; Launey et al. 2010). Understanding how different length scales impart these mechanical properties is essential in the field of tissue engineering and for the design of bioinspired materials (Wegst et al. 2015; Yang et al. 2018; Santulli 2015). Therefore, several studies have been dedicated to elucidating the mechanical behavior of bone at different scales, among which we can mention (Hamed et al. 2010; Martínez-Reina et al. 2011; Sabet et al. 2016).

At the sub-micron scale, the bone is composed of mineralized collagen fibrils with diameters ranging from 80–100 nm, surrounded by fine hydroxyapatite (HA) mineral crystals (Weiner and Wagner 1998). Mechanical properties of collagen fibrils have widely been studied via atomic force microscopy (AFM) (Yang et al. 2008; Shen et al. 2008; Wenger et al. 2007; Yang 2008; Hang and Barber 2011) and

✉ Soheil Soghrati
soghrati.1@osu.edu

¹ Department of Mechanical and Aerospace Engineering, The Ohio State University, 201 West 19th Avenue, Columbus, OH, USA

² Department of Biomedical Engineering, The Ohio State University, 201 West 19th Avenue, Columbus, OH, USA

³ Software Development Engineer, Amazon, Seattle, USA

⁴ Department of Materials Science and Engineering, The Ohio State University, 201 W. 19th Avenue, Columbus, OH, USA

modeled using the finite element method (FEM) (Jäger and Fratzl 2000; Sanchez 2013). However, due to the complexity of the bone internal architecture at such a small scale, proper characterization of its nanostructure is a challenging task (Weiner and Traub 1992) that has been the subject of several studies in recent years, some resulting in contradictory outcomes. In some studies, it has been concluded that the mineral phase is only present in the gap zones of collagen fibrils (Landis et al. 1996; Weiner et al. 1991; Tong et al. 2003). However, some recent studies have suggested that more than 70% of minerals is extra fibrillar, where mineral platelets are surrounding collagen fibrils in a shell-like fashion (McNally et al. 2012, 2013). On the other hand, there are studies indicating that mineral platelets further aggregate into more complex, irregular structures around collagen fibrils (Reznikov et al. 2018).

These complexities have entailed the use of simpler models such as 2D finite element (FE) models (Schwarcz et al. 2017; Ji and Gao 2004; Bar-On and Wagner 2011) to study the bone stiffness and strength at the sub-micron scale, assuming that minerals are arranged in a staggered manner in a collagen matrix. This arrangement has also been adopted in a 3D FE model to study the bone stiffness in Vercher et al. (2014), as well as in several analytical studies (Zhang et al. 2010; Bar-On and Wagner 2011). The Mori-Tanaka homogenization approach has also been employed to study the bone stiffness at this scale (Nikolov and Raabe 2008). More recent studies have used Voronoi tessellation to generate the 3D collagen-mineral platelet arrangement to investigate the toughening mechanisms at the submicron scale (Wang et al. 2018). Damage simulations at this scale have also been carried out to identify the effect of spatial arrangement and diameters of collagen fibrils on the fracture toughness (Wang and Ural 2018).

One of the remarkable characteristics of bone is its piezoelectricity, arising primarily from the organic component (collagen fibrils) (Marino et al. 1971; Tofail et al. 2011). Since the first experimental characterization of the bone piezoelectricity (Fukada and Yasuda 1964), it has drawn significant attention as a transduction mechanism to explain the bone adaptivity to external loadings. More specifically, the positive charge on the collagen surface piezoelectrically generated in response to external loadings may attract negatively charged ion clusters of calcium phosphate; thus collagen piezoelectricity is possibly one of the main contributors to mediate the bone mineralization process. The fact that the collagen piezoelectricity exhibits anisotropic properties makes it more appealing to adapt various types of loading, such as axial compression, bending, twisting, and shear (Kalinin et al. 2006; De Jong et al. 2015). Although the piezoelectric property of bone has been experimentally characterized at the macroscale (Fukada and Yasuda 1964; Gjelsvik 1973; Bassett 1965) and single-fibrillar scale (i.e.,

nanoscale) (Minary-Jolandan and Yu 2009; Denning et al. 2017), the physiological importance of the collagen piezoelectricity has not been fully elucidated. To fill the gap, it is important to understand how the electric field is generated under various loading conditions considering the anisotropic piezoelectric properties of collagen fibrils. Performing such study also requires taking into account the impact of the complex heterogeneous structure of the bone at the sub-micron scale.

While a number of computational studies have been carried out to link the bone nanostructure to its mechanical behavior and failure response, to the best of the authors' knowledge, no study exists on numerical analysis of the bone piezoelectric response at this scale. In this manuscript, we present an automated computational framework for the virtual reconstruction, FE modeling, and simulating the piezoelectric response of the bone at the submicron scale. We introduce a new reconstruction algorithm relying on the Centroidal Voronoi Tessellation (CVT) algorithm and Non-Uniform Rational B-Splines (NURBS) to synthesize 3D models of the bone nanostructure considering the misalignment between collagen fibrils. Four virtual models with various volume fractions, spatial arrangement, and spatial orientation of collagen fibrils are then reconstructed to study the impact of the nanostructures on the piezoelectric response of the bone. A parallel version of the meshing algorithm Conforming to Interface Structured Adaptive Mesh Refinement (CISAMR) is employed to create a high-fidelity FE model for each nanostructure. A static piezoelectric model is then utilized to simulate the response of bone nanostructures under three different loading conditions, namely compression in the longitudinal and transverse fibers direction, as well as transverse shear.

The remainder of this manuscript is organized as follows. The formulation of the problem at the sub-micron scale is presented in Sect. 2. The CVT-NURBS reconstruction algorithm is introduced in Sect. 3, followed by an overview of the CISAMR algorithm for creating 3D FE models. A detailed discussion on piezoelectric response of the nanostructure along with its implications to bone remodeling is provided in Sect. 4. Final concluding remarks are summarized in Sect. 5.

2 Problem formulation

2.1 Governing equations

In this section, we introduce the equations governing the piezoelectric response of materials under the assumptions of a small electric field and linear elastic material behavior (Madarash-Hill and Hill 2004). In the absence of body forces, the constitutive equations must simultaneously take

into account the mechanical equilibrium and the conservation of electric flux as

$$\epsilon_{ij} = S_{ijkl}^E \sigma_{kl} - d_{mij}^\psi E_m, \quad (1)$$

$$q_i = d_{ijk}^\psi \sigma_{jk} + D_{ij}^\sigma E_j, \quad (2)$$

where σ_{ij} is the Cauchy stress tensor, q_i is the electric displacement vector (electric flux density), S_{ijkl}^E is the fourth-order material compliance tensor, d_{mij}^ψ is the piezoelectric constant tensor, D_{ij}^σ is the dielectric constant tensor. The strain tensor ϵ_{kl} and the electric field vector E_m are evaluated based on nodal displacements and electric potential obtained from the FE approximation, respectively. The constitutive equations (1) and (2) are solved in conjunction with the mechanical equilibrium and flux conservation equations, which are integrated over the FE mesh. Note that in this work, only collagen fibrils exhibit a piezoelectric response, meaning corresponding constants do not need to be defined for the non-piezoelectric mineral phase.

Assume Θ is a Statistical Volume Element (SVE) of the bone at the sub-micron scale defined in the coordinate system \mathbf{x}_m , with boundary Λ and outward unit normal vector \mathbf{n}_m . Characteristic length scales of the upper-scale domain Ω and the lower-scale Θ are denoted by l_M and l_m , respectively. In order to implement the theory of homogenization, these length scales must satisfy

$$\xi = \frac{l_m}{l_M} \ll 1, \quad (3)$$

which ensures the effect of boundary conditions imposed on Θ on resulting homogenized properties is negligible (assumption of constant macroscopic stress/strain). The Hill-Mandel micro-homogeneity principle at a given macroscopic point can then be written as (Hill 1985)

$$\inf_{\mathbf{u}_M} \Phi_M(\epsilon_M) = \inf_{\epsilon_M} \inf_{\mathbf{u}_m} \frac{1}{|\Theta|} \int_{\Theta} \Phi_m(\epsilon_M + \epsilon_m) d\Theta, \quad (4)$$

where $\Phi_M = \frac{1}{2} \epsilon_M : \sigma_M$ is the macroscopic energy density at that point and $\Phi_m = \frac{1}{2} (\epsilon_M + \epsilon_m) : \sigma_m$ is the average microscopic energy density in Θ , *i.e.*, the microscopic domain of corresponding SVE. Here, ϵ_m and σ_m denote the microscopic strain and stress tensors, respectively.

After evaluating the response of an SVE (ϵ_m and σ_m), the homogenized strain tensor at the corresponding macroscopic point can be evaluated using the strain averaging theorem as

$$\epsilon_M(\mathbf{x}_M) = \frac{1}{|\Theta|} \int_{\Theta} \epsilon_m(\mathbf{x}_m) d\Theta. \quad (5)$$

Similarly, the macroscopic stress tensor and the electric field vector at this point are given by

$$\sigma_M(\mathbf{x}_M) = \frac{1}{|\Theta|} \int_{\Theta} \sigma_m(\mathbf{x}_m) d\Theta, \quad (6)$$

$$\mathbf{E}_M(\mathbf{x}_M) = \frac{1}{|\Theta|} \int_{\Theta} \mathbf{E}_m(\mathbf{x}_m) d\Theta. \quad (7)$$

Note that the assumption of linear behavior allows for the superposition of the response of the two phases (Martínez-Ayuso et al. 2017).

3 Automated modeling framework

The bone nanostructure is composed of mineralized collagen fibrils with an average diameter of ~ 100 nm surrounded by a mineral phase. Based on the tomography reconstruction of the bone at this scale presented in McNally et al. (2013) (Fig 5a, p. 51), shows the mineral phase surrounding collagen fibrils in a shell-like fashion. A simplified geometrical model of this complex nanostructure taken from McNally et al. (2012) is illustrated in Fig. 1a, showing stacks of mineral plates surrounding each fibril, as well as voids at junctions of mineral stacks associated with neighboring fibrils. Such voids can also be discerned in the tomography image from McNally et al. (2013) as pores that are significantly smaller than diameter of collagen fibrils. Based on these interpretations, we aim to virtually reconstruct 3D models of the bone nanostructure consisting of aligned/misaligned collagen fibrils embedded in a porous mineral matrix. Figure 1b shows a sample SVE reconstructed using the algorithm developed for this purpose and described in the remainder of this section. Note that the bone architecture at this scale is even more complex, *e.g.*, the mineral phase is composed of mineral platelets. However, because in this study we are not concerned with local phenomena such as damage and instead aim to approximate the homogenized piezoelectric response of the bone, which is averaged over the entire domain, the assumption made for the reconstruction of an SVE model similar to that shown in Fig. 1b are reasonably realistic.

The proposed algorithm for the virtual reconstruction of bone SVEs at the sub-micron scale consists of three main phases: (i) a modified Centroidal Voronoi Tessellation (CVT) (Du et al. 1999) to create 2D cross sections of collagen fibrils embedding within Voronoi cells (Sect. 3.1); (ii) adding voids at Voronoi vertices (Sect. 3.2); and (iii) extruding fibrils and voids Non-Uniform Rational B-Splines (NURBS) representation to create the 3D geometrical model (Sect. 3.3). Note that the CVT algorithm was chosen for reconstructing the bone nanostructure to avoid the clustering of collagen fibrils, which allows replicating in a relatively uniform distribution of fibrils, as seen in healthy bone

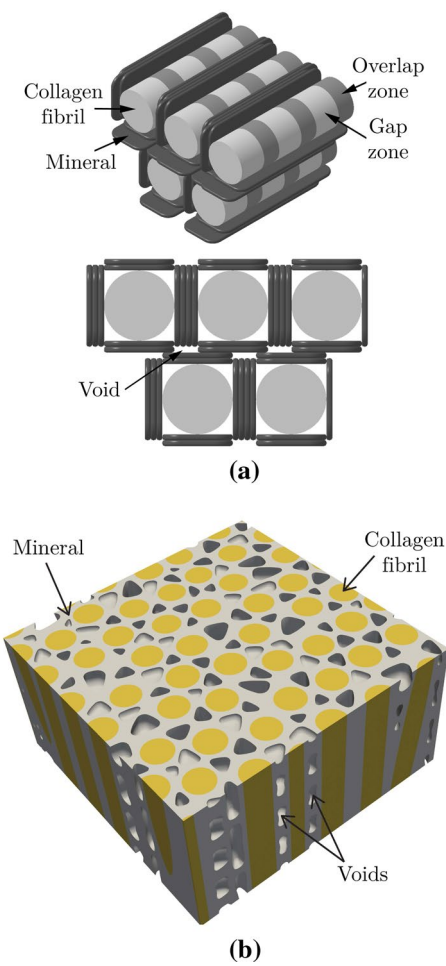


Fig. 1 **a** Simplified geometrical model, including collagen fibrils and mineral platelets (figure adopted from (McNally et al. 2012)); **b** SVE virtually reconstructed using the algorithm introduced in this work

tissue. More importantly, this algorithm facilitates adding misaligned fibrils to the bone nanostructure by providing more control on the placement of each fibril and its relative distances to neighboring fibrils. Further, CVT enables embedding voids in the mineral phase without overlapping with existing fibrils using vertices/edges of Voronoi cells to determine locations of these voids. Next, we describe each phase in more detail.

3.1 Reconstruction of collagen fibrils

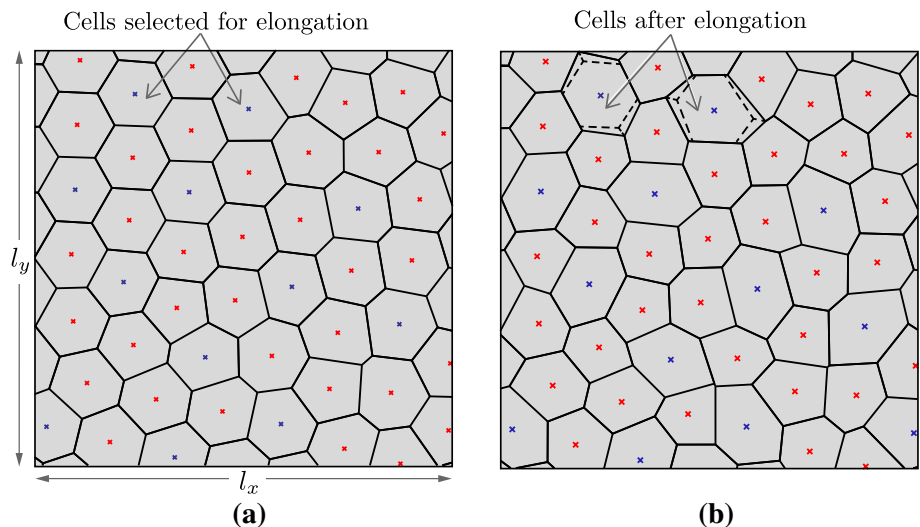
In order to virtually reconstruct the bone nanostructure, we first create a 2D rectangular domain with lengths l_x and l_y that represents a cross section perpendicular to the principal collagen fibrils direction. This 2D domain is discretized using the CVT algorithm, which begins by implementing the Voronoi tessellation using randomly generated seed points. The number of seed points, N_{sp} , determines the number of collagen fibrils, which is evaluated based on their desired volume fraction V_f as

$$N_{sp} = \frac{l_x l_y V_f}{\pi r^2}, \quad (8)$$

where r is the average radius of collagen fibrils, assumed to be 50 nm in this study. However, the random spatial arrangement of seed points in the 2D domain prohibits insertion of collagen fibril without avoiding overlaps between them. Thus, we iteratively relocate seed points to centroids of their corresponding Voronoi cells until reaching a uniform distribution of seed points and Voronoi cells with roughly the same size, as shown in Fig. 2a.

The seed points generated using the CVT algorithm serve as initial centroids for the insertion of straight and misaligned collagen fibrils (*c.f.* Fig. 2a and b, ensuring no

Fig. 2 **a** Voronoi cells generated using the CVT algorithm to create the raw nanostructure with cells selected for elongation are marked with blue centroids; **b** Voronoi cells after the elongation of cells holding misaligned fibrils. Two of the original cells before the elongation are shown using dashed lines



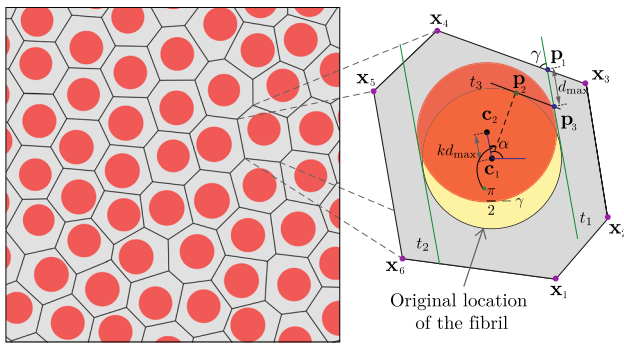


Fig. 3 (Left) Raw nanostructure created using CVT-based algorithm where fibrils are perfectly aligned; (right) geometric illustration of the maximum movement algorithm

overlap between them as far as the circular cross section of each fibril is confined within each Voronoi cell. However, this results in a highly uniform spatial arrangement of collagen fibrils (no clustering), which is not realistic. Therefore, in order to introduce more randomness in the SVE nanostructure, the center point of each fibril is relocated from the centroid \mathbf{c}_1 of the Voronoi cell (seed point) to a new

point \mathbf{c}_2 within the Voronoi cell at a randomly selected angle $0 < \alpha < 2\pi$. The distance between \mathbf{c}_1 and \mathbf{c}_2 is a randomly chosen fraction k of the maximum allowable distance, d_{\max} , that the fibril can move in the selected direction without intersecting Voronoi walls, as shown in Fig. 3. The step-by-step process of evaluating d_{\max} is as follows:

1. Evaluate the equations of tangents t_1 and t_2 to the fibril's cross section that form the angle α with the x -axis.
2. Calculate intersection points of t_1 and t_2 with the Voronoi walls; then locate the intersection point \mathbf{p}_1 (In Fig. 3, corresponding to t_1) with the smallest distance from \mathbf{c}_1 . Also, identify the Voronoi edge $\mathbf{x}_3 - \mathbf{x}_4$ holding \mathbf{p}_1 and its angle γ with tangent t_1 .
3. Find point \mathbf{p}_2 located on the fibril circular cross section such that the radius passing through that makes angle $\frac{\pi}{2} - \gamma$ with $\mathbf{c}_1\mathbf{c}_2$. Note that the tangent t_3 passing through \mathbf{p}_2 is parallel to the Voronoi edge $\mathbf{x}_3 - \mathbf{x}_4$.
4. The maximum allowable distance for relocating the collagen fibril is calculated as $d_{\max} = \|\mathbf{p}_3 - \mathbf{p}_1\|$, where \mathbf{p}_3 is the intersection point of tangents t_1 and t_3 (cf. Fig. 3). The pseudocode for calculating d_{\max} is presented in Algorithm 1.

Algorithm 1 (Evaluating maximum allowable distance, d_{\max} , for moving a fibril in a Voronoi cell)

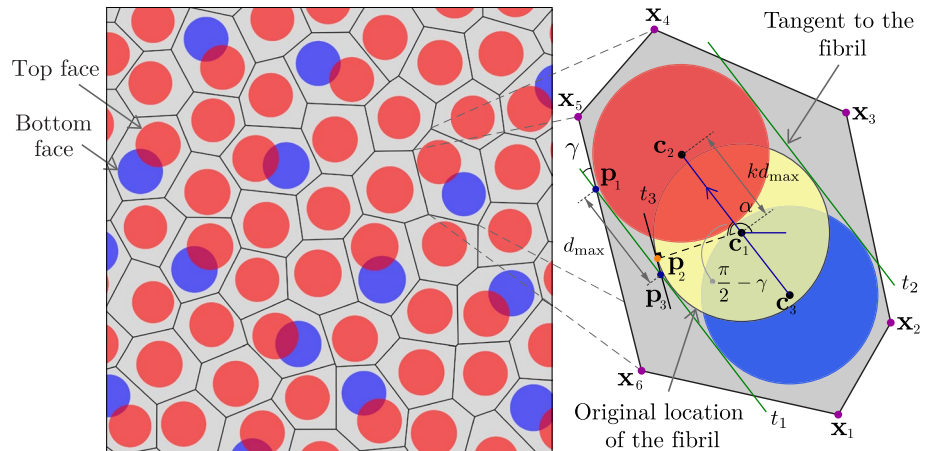
```

1: function MAX_DIST( $\mathbf{c}_1, r, \alpha, \mathbf{x}$ )
2:    $t_1, t_2 \leftarrow \text{tangent\_finder\_1}(\mathbf{c}_1, r, \alpha)$ 
3:    $\mathbf{x}_i, \mathbf{x}_j \leftarrow \text{edge\_locator}(t_1, t_2, \mathbf{x})$ 
4:    $\mathbf{p}_{t_1}, \mathbf{p}_{t_2} \leftarrow \text{int\_points}(t_1, t_2, \mathbf{x}_i, \mathbf{x}_j)$ 
5:    $\mathbf{p}_1 \leftarrow \text{min\_dist}(\mathbf{p}_{t_1}, \mathbf{p}_{t_2}, \mathbf{c}_1)$ 
6:    $\gamma \leftarrow \text{angle}(\mathbf{x}_i, \mathbf{x}_j, t_1)$ 
7:    $\mathbf{p}_2 \leftarrow \text{point\_locator}(\gamma, \mathbf{c}_1, r)$ 
8:    $t_3 \leftarrow \text{tangent\_finder\_2}(\mathbf{c}_1, r, \mathbf{p}_2)$ 
9:    $\mathbf{p}_3 \leftarrow \text{find\_intersection}(t_1, t_3)$ 
10:   $d_{\max} \leftarrow \text{dist}(\mathbf{p}_1, \mathbf{p}_3)$ 
11: end function

```

▷ Find tangents t_1, t_2 to fibril forming angle α with x -axis
 ▷ Locate vertices \mathbf{x}_i and \mathbf{x}_j of Voronoi edges intersecting with t_1, t_2
 ▷ Calculate intersections of t_1 and t_2 with Voronoi edges
 ▷ Find intersection point \mathbf{p}_1 with minimum distance to \mathbf{c}_1
 ▷ Find angle between edge holding \mathbf{p}_1 and corresponding tangent t_1
 ▷ Find \mathbf{p}_2 on fibril, whose radius forms angle $\frac{\pi}{2} - \gamma$ with $\mathbf{c}_1\mathbf{c}_2$
 ▷ Find tangents t_3 to fibril that passes through point \mathbf{p}_2
 ▷ Find intersection point between tangents t_1 and t_3
 ▷ Calculate d_{\max} as distance between points \mathbf{p}_1 and \mathbf{p}_3

Fig. 4 Raw nanostructure created using CVT-based algorithm, showing the top (red) and bottom (blue) faces of collagen fibrils, together with the geometric illustration of the maximum movement algorithm to introduce misalignment in an elongated Voronoi cell



The relocation algorithm described above can be used to create the misalignment of collagen fibrils by moving a fibril from its original location in directions α and $2\pi - \alpha$, which can represent the top and bottom faces of the fibril in the final 3D SVE (*cf.* Fig. 4). Note that because both relocated positions are still within the walls of each Voronoi cells, there will be no overlap between neighboring fibrils. However, especially when attempting to reconstruct SVEs with a high volume fraction of collagen fibrils, it is not feasible to create fibrils with a notable misalignment (*e.g.*, $> 5^\circ$) as there is not much room for moving each fibril within its Voronoi cell. Recall that the cells generated using the CVT algorithm have roughly the same size, which shrinks with increasing the fibrils volume fraction.

In order to increase the feasible range of fibrils misalignment in the virtual SVE, prior to using the relocation algorithm for creating top/bottom faces of each fibril, we elongate certain Voronoi cells to create more room for this task. In this approach, the cells are first sorted based on the length

of their longest diagonal. The cells with the longest diagonals are then selected and corresponding vertices are moved apart (*c.f.* Fig. 2b) to create more space for a misaligned fibril. Note that two neighboring cells cannot be selected for elongation, as it might distort the shape of an already elongated cell. The centers of circles corresponding to the two faces of the fibrils can then be offset to incorporate the misalignment. To maximize the angle of misalignment, the maximum movement scheme presented in Algorithm 1 is used in directions with angles α and $2\pi - \alpha$. However, rather than being a randomly chosen angle, α corresponds to the angle of the longest diagonal of the elongated cell with the x -axis (*cf.* Fig. 4). The pseudocode for the reconstruction of a 2D cross section of the bone nanostructure considering the presence of misaligned collagen fibrils is presented in Algorithm 2. Note that this algorithm allows creating collagen fibrils with up to 20° misalignment in the longitudinal fibrils direction.

Algorithm 2 (Reconstructing virtual 2D SVE with misaligned collagen fibrils)

```

1: function GENERATE_FIBRILS( $V_f, MA, R$ )
2:    $v_i, C_i \leftarrow \text{cvt}(V_f)$                                  $\triangleright$  Generate fibrils based on desired volume fraction
3:   if  $MA == \text{true}$  then                                      $\triangleright$  Generate CVT based on the desired volume fraction  $V_f$ 
4:      $C_i \leftarrow \text{sort\_longest\_diagonal}(C_i, v_i)$             $\triangleright$  Check if fibril misalignment is desired
5:     for ( $C_i = C_i(\text{begin}); C_i \neq C_i(\text{end}); C_i++$ ) do     $\triangleright$  Sort cells w.r.t. longest diagonals of the cells
6:       if neighbor_elongated() then                                 $\triangleright$  Check if neighboring cell is already elongated
7:         continue_for_loop()
8:       end if
9:        $C_i \leftarrow \text{elongate\_cell}(C_i, v_i)$                        $\triangleright$  Elongate cells whose neighbors are not elongated
10:      end for
11:    end if
12:    for ( $C_i = C_i(\text{begin}); C_i \neq C_i(\text{end}); C_i++$ ) do     $\triangleright$  Select radius based on average desired radius  $R$ 
13:       $r_i \leftarrow \text{radius\_selector}(R)$                             $\triangleright$  Generate fibril at center of the cell
14:       $c_i \leftarrow \text{generate\_fibril}(r_i, C_i)$ 
15:      if elongated then                                          $\triangleright$  Select  $\alpha$  in longest diagonal direction and relocation fraction  $k$ 
16:         $\alpha, k \leftarrow \text{move\_selector}()$                           $\triangleright$  misalign fibril using  $d_{\max}$  algorithm at  $\alpha$  and  $2\pi - \alpha$ 
17:         $c_i \leftarrow \text{misalign\_fibril}(\alpha, k, c_i, C_i)$ 
18:        continue_for_loop()
19:      end if
20:       $\alpha, k \leftarrow \text{move\_selector}()$                           $\triangleright$  randomly select relocation angle  $\alpha$  and fraction  $k$ 
21:       $c_i \leftarrow \text{move\_fibril}(\alpha, k, c_i, C_i)$                  $\triangleright$  Move fibril using maximum movement algorithm
22:    end for
23: end function

```

3.2 Creating voids cross sections

After creating the fibrils' upper/lower surfaces in the 2D nanostructure, we must incorporate the voids in its mineral matrix. In this 2D cross section, the voids are generated at vertices of Voronoi cells, which are surrounded by three collagen fibrils (cf. Fig. 5a). First, we generate a triangular bound for each void to ensure it does not overlap with existing fibrils. For a Voronoi vertex v surrounded by three fibrils centered at $\mathbf{c}_1, \mathbf{c}_2$, and \mathbf{c}_3 and connected to Voronoi edges $\mathbf{l}_{12}, \mathbf{l}_{23}$ and \mathbf{l}_{13} , the triangular void bound is generated as follows:

1. Find intersection points \mathbf{p}_{ij} of line segments \mathbf{c}_i and \mathbf{c}_j ($i, j = 1, 2, 3$) with each of the shared edges \mathbf{l}_{ij} (green nodes in Fig. 5a).
2. Evaluate the distance between each line segment connecting resulting intersection points to centers of corresponding circles representing a fibril cross section. This distance is used to determine whether the triangular bound is too close/intersecting with any of the fibril cross sections. For example, in Fig. 5a, the initial bound is too close to the circle centered at \mathbf{c}_1 .
3. If the distance between an edge and a fibril is too small, move that edge inward parallel to itself such that the corresponding distance becomes more than ≈ 20 nm (20% of average fibril diameter). For example, in Fig. 5a, the edge connecting intersecting points \mathbf{p}_{13} and \mathbf{p}_{12} is relocated to increase the distance between the edge connecting them to the fibril centered at \mathbf{c}_1 .

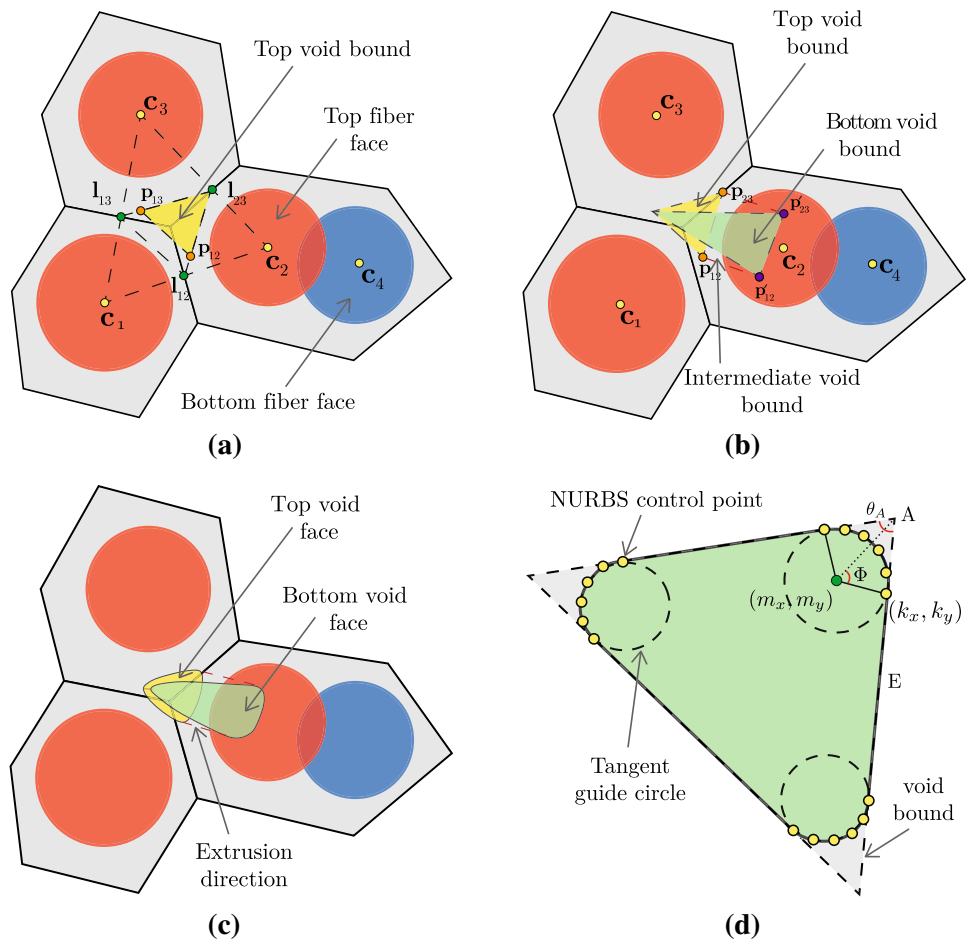
The algorithm above generates the 2D bound of an *aligned void*, *i.e.*, a void surrounded by three aligned collagen fibrils. To more realistically represent a void cross section and eliminate sharp vertices of triangular void bounds, which cause difficulty in creating a high-quality conforming mesh and introduce unrealistic stress concentrations, we smoothen this shape by filleting its corners. As shown in Fig. 5d, in order to smoothen vertex A of a triangular bound, we replace this vertex and portions of edges connected to that with a circular arc of radius r . First, we generate point (k_x, k_y) on edge E with length l at distance $0.2l < d < 0.3l$ from vertex A. The center of the circle must be placed at point (m_x, m_y) such that edge E is tangent to it at point (k_x, k_y) . Note that the angle between the lines connecting this center point to vertex A and perpendicular to edge E is $\Phi = \frac{\pi}{2} - \frac{\theta_A}{2}$, where θ_A is the angle at vertex A. The radius of the circle can then be evaluated as $r = d \cot \Phi$, which can be used to determine the coordinate of (m_x, m_y) , *i.e.*, a point at distance r from (k_x, k_y) and perpendicular to E. Finally, the additional 5 points shown in yellow in Fig. 5d are generated on the circular arc, where the coordinate $(g_x^{(j)}, g_y^{(j)})$ of the j th point ($j = 1$ to 5) is evaluated as

$$g_x^{(j)} = m_x + (k_x - m_x) \cos \alpha_j - (k_y - m_y) \sin \alpha_j, \quad (9)$$

$$g_y^{(j)} = m_y + (k_y - m_y) \cos \alpha_j + (k_x - m_x) \sin \alpha_j, \quad (10)$$

$$\text{where } \alpha_j = \frac{2j}{5}\Phi.$$

Fig. 5 **a–c** Process of generating the morphology of the top and bottom faces of a misaligned void, which requires **d** transforming an initial void bound into a void face by creating proper NURBS control points



Additional steps are required to virtually reconstruct a *misaligned void*, *i.e.*, a void surrounded by at least one misaligned collagen fibril. In such cases, we first create the void bound with respect to one of the top/bottom fibril faces that is closer to the selected Voronoi vertex. Referring to Fig. 5a, assume the circles centered at c_2 and c_4 represent the top and bottom faces of a misaligned fibril, respectively. The initial void bound is created with respect to the face closer to the Voronoi vertex (in this case, the circle centered at c_2). Therefore, the void bound created using this approach corresponds to one of the faces of the misaligned fibril (here, the top face at c_2). To generate the void bound corresponding to the farther face of the fibril (bottom face), we create the

edge $p'_{12}-p'_{23}$ parallel to and with the same length as $p_{12}-p_{23}$ at a distance of 20 nm to 30 nm from the bottom face of the fibril. As shown in Fig. 5b, edge $p'_{12}-p'_{23}$ is used to create the triangular bound for the bottom face of the misaligned void. Subsequently, the two triangular bounds are smoothed using the algorithm outlined in the paragraph above to form the top and bottom faces of the void, as shown in Fig. 5c.

3.3 NURBS representation of fibrils and voids

After incorporating the voids in the 2D nanostructure shown in Fig. 4, we must extrude that into a 3D geometrical model of the bone considering the presence of misaligned collagen fibrils and voids. Note that while the collagen fibrils are

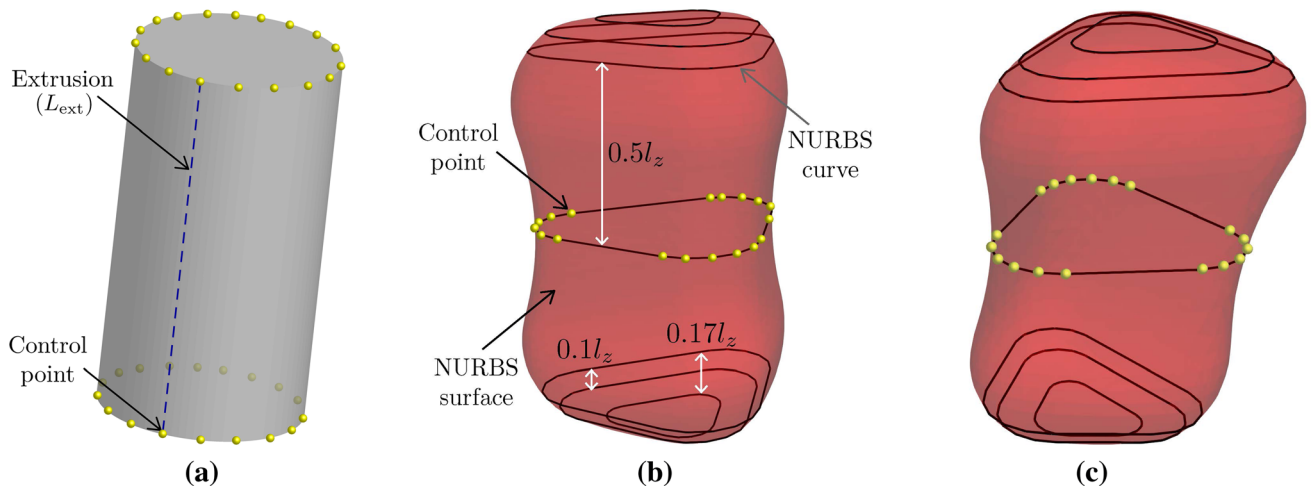


Fig. 6 Using NURBS curve extrusion to reconstruct the 3D morphology of **a** collagen fibril; **b** aligned void; and **c** misaligned void

modeled as continuous fibers, one must take into account the discrete nature of voids in the longitudinal fibrils direction (*i.e.*, along z -axis). In this work, we use Non-Uniform Rational B-Splines (NURBS) (Piegl and Tiller 2012) to represent the geometry of both the collagen fibrils and the voids. A NURBS curve, $\mathbf{C}(u)$, is a parametric function that can represent complex geometries using a set of n B-splines of order p , $M_i^p(u)|_{i=1}^n$, where u is the parametric coordinate. $\mathbf{C}(u)$ is evaluated by interpolating B-spline functions at n control points with physical (Lagrangian) coordinates \mathbf{x}_i as

$$\mathbf{C}(u) = \sum_{i=1}^n \frac{\mathbf{x}_i w_i M_i^p(u)}{\sum_{j=1}^n w_j M_j^p(u)}, \quad (11)$$

where w_i is the weight assigned to each control point.

Given the cylindrical shape of collagen fibrils, their NURBS representation is rather straightforward. First, we create 21 equally distanced control points on the top face of each fibril to characterize its circular shape using a third-order 2D NURBS curve. This curve is then extruded along the line segment L_{ext} connecting circumferential points of top and bottom faces of the fibril, resulting in a 3D NURBS surface, as shown in Fig. 6a. Note that the NURBS extrusion is a straightforward task that only requires specifying coordinates of control points along the extrusion curve (here, the top and bottom faces of fibrils).

The virtually reconstructed top and bottom void faces must also be extruded in the z direction to generate discrete 3D voids, each with a randomly selected length of $40 \text{ nm} < l_z < 100 \text{ nm}$ in this direction. The points created for smoothening triangular void bounds, *i.e.*, (k_x, k_y) and

$(g_x^{(j)}, g_y^{(j)})$, are given as NURBS control points in this case. Evaluating the 3D NURBS parameterization of an aligned void is rather straightforward, where identical top and bottom NURBS for faces reconstructed in the xy plane can be extruded to generate the void geometry. However, this simplistic approach yields voids with uniform cross sections and flat top/bottom faces, which is not realistic. To avoid this issue, in addition to identical 2D NURBS curves representing top/bottom faces of a void at distance l_z , we create another copy of this curve in the z direction at distance $0.5l_z$ from both these faces (*cf.* Fig. 6b). We also create two additional copies of the NURBS curve corresponding to the top (bottom) face, shrunk by 14% and 50% with respect to its centroid, and place them at distances $0.1l_z$ and $0.17l_z$ further to the top (bottom) of this face, respectively. The shape of 3D NURBS representation of an aligned void created by extruding the 7 NURBS curve created using this approach is illustrated in Fig. 6b.

The algorithm above must be modified to enable creating the 3D NURBS representation of misaligned voids, as shown in Fig. 6c. Similar to an aligned void, the extrusion algorithm requires creating 5 new NURBS curves in the xy plane in addition to those previously generated for the top and bottom faces. For the middle curve at distance $0.5l_z$, we must first generate an appropriate void bound and then transform that into a smoothed NURBS. This is achieved using a similar algorithm as that described in Sect. 3.2 for creating the void bound for the bottom face, *i.e.*, by sliding edge $\mathbf{p}_{12}-\mathbf{p}_{23}$ along the misaligned fibril to create edge $\mathbf{p}'_{12}-\mathbf{p}'_{23}$ (*cf.* Fig. 5b). The edge $\mathbf{p}'_{12}-\mathbf{p}'_{23}$ of the misaligned fibril is generated by sliding $\mathbf{p}_{12}-\mathbf{p}_{23}$ by distance $0.5l_z$ in the z direction along the same oblique angle, followed by creating the void bound and then the corresponding NURBS curve at this location. The remaining 4 planar NURBS curves are

generated with similar scale-down factors (14% and 50%) and distancing in the z direction ($0.1l_z$ and $0.17l_z$) as those used for creating aligned voids by applying offsets with respect to the top and bottom faces of the void in the xy plane to take into account the effect of misalignment.

The pseudocode for creating the NURBS representation of voids in the proposed reconstruction algorithm is presented in Algorithm 3. Figure 7 shows two bone SVEs virtually reconstructed using this algorithm with fibril volume fractions $V_f = 45.7\%$ (aligned) and $V_f = 39.0\%$ (misaligned).

Algorithm 3 (Reconstruction of void geometries)

```

1: function VOID_GENERATOR( $C_i, V_i$ )
2:   for ( $V_i = V_i(\text{begin})$ ;  $V_i \neq V_i(\text{end})$ ;  $V_i++$ ) do
3:      $n_l \leftarrow \text{layers\_selector}(S_f)$ 
4:      $S_v, C_v \leftarrow \text{get\_connectivity}(V_i, C_i)$ 
5:      $c_v, r_v \leftarrow \text{get\_fibril\_data}(C_v)$ 
6:     if elongated == true then
7:        $c_v, r_v \leftarrow \text{get\_nearest\_center}()$ 
8:        $P_v \leftarrow \text{get\_intersection}(c_v, S_v)$ 
9:       dist  $\leftarrow \text{eval\_dist}(c_v, r_v, P_v)$ 
10:      if dist < tol then
11:         $P_v \leftarrow \text{update\_segment\_points}(P_v)$ 
12:      end if
13:       $c_v, r_v \leftarrow \text{get\_second\_center}()$ 
14:      if dist > 2tol then
15:         $P_v \leftarrow \text{update\_segment}(P_v)$ 
16:      end if
17:      dist  $\leftarrow \text{eval\_dist}(C_j, R_j, P_j)$ 
18:       $\mathbf{x}_v \leftarrow \text{create\_fillet}(P_v)$ 
19:       $\mathbf{x}_v \leftarrow \text{extrude}(\mathbf{x}_v, n_l)$ 
20:       $\mathbf{x}_v \leftarrow \text{round\_end}(\mathbf{x}_v, n_l)$ 
21:    else
22:       $P_v \leftarrow \text{get\_intersection}(c_v, S_v)$ 
23:      dist  $\leftarrow \text{eval\_dist}(c_v, r_v, P_v)$ 
24:      if dist < tol then
25:         $P_v \leftarrow \text{update\_segment\_points}(P_v)$ 
26:      end if
27:       $\mathbf{x}_v \leftarrow \text{create\_fillet}(P_v)$ 
28:       $\mathbf{x}_v \leftarrow \text{extrude}(\mathbf{x}_v, n_l)$ 
29:       $\mathbf{x}_v \leftarrow \text{round\_end}(\mathbf{x}_v, n_l)$ 
30:    end if
31:  end for
32: end function

```

▷ Loop over each vertex of the voronoi cells

▷ Select number of voids in z direction for each voronoi vertex

▷ Get edges and cells connected to the vertices

▷ Get centers and radius of the fibrils surrounding the vertex

▷ Check if adjacent cell is elongated

▷ Update centers with that of nearest profile to vertex

▷ Intersection of edges and line connecting fibril centers

▷ Find distance between the intersection points and fibrils

▷ Move void bound closer to the fibril further from it

▷ Update centers with that of farther profile to vertex

▷ Move void bound far from the farther fibril profile closer

▷ Fillet the triangular void bound

▷ Extrude to get n_l 3D voids

▷ Round the void ends to get final NURBS

▷ Intersection of edges and line connecting fibril centers

▷ Find distance between the intersection points and fibrils

▷ Move void bound closer to the fibril further from it

▷ Fillet the triangular void bound

▷ Extrude to get n_l 3D voids

▷ Round the void ends to get final NURBS

Fig. 7 Two $800 \text{ nm} \times 800 \text{ nm} \times 400 \text{ nm}$ bone SVEs synthesized using the proposed CVT-NURBS reconstruction algorithm. Note that for more clarity, rather than the mineral matrix, the figure illustrates the voids present in this phase

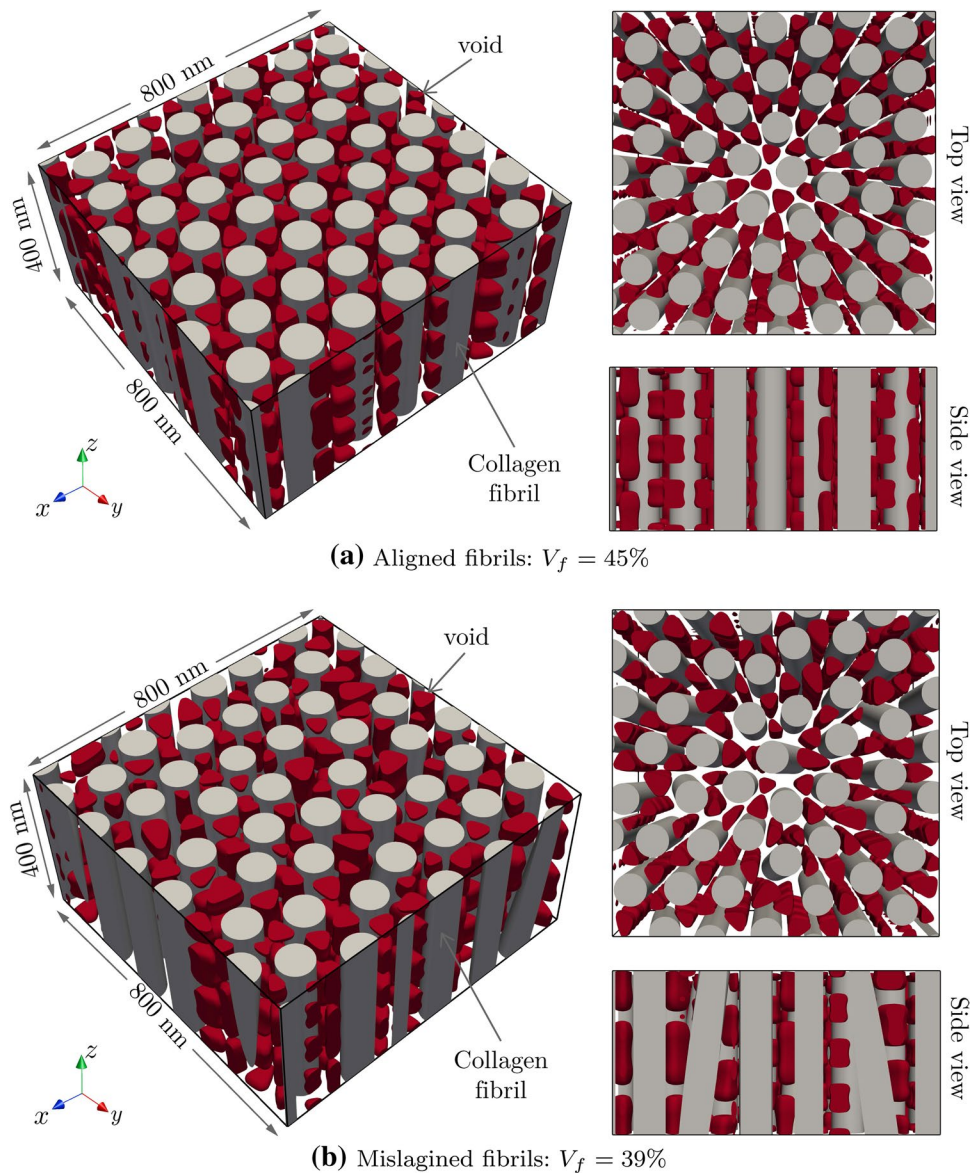


Table 1 Material properties of collagen fibrils and the mineral phase

Material	E (GPa)	ν	D (F m^{-1})
Collagen	2.4 (Hang and Barber 2011)	0.3	50×10^{-12} (Kaygili et al. 2014)
Mineral	80 (Yuan et al. 2011)	0.28	95×10^{-12} (Tomaselli and Shamos 1973)

3.4 Mesh generation

The virtually reconstructed SVEs must then be transformed into high-quality conforming FE meshes to simulate their piezoelectric response under different loading conditions. In this work, we implement the Conforming to Interface Structured Adaptive Mesh Refinement (CISAMR) (Soghrati et al. 2017; Nagarajan and Soghrati 2018) algorithm to generate the FE models. CISAMR is a non-iterative meshing algorithm that transforms a structured background mesh (composed of tetrahedral elements) into an adaptively refined conforming mesh ensuring that the aspect ratio of resulting elements is less than 5. As shown in Fig. 8, this transformation occurs in four steps: (i) h -adaptive refinement of background elements intersecting the material interface; (ii) r -adaptivity of nodes of background elements cut by the interface, during which some of these nodes are relocated to the interface; (iii) face-swapping to eliminate cap/sliver-shaped tetrahedrons with a high aspect ratio that might emerge after performing r -adaptivity; and (iv) sub-tetrahedralization of nonconforming background elements, as well as elements with hanging nodes (created during the h -adaptive refinement phase) to generate the final conforming mesh. A detailed description of each phase of the 3D CISAMR algorithm is presented in Nagarajan and Soghrati (2018).

Figure 9 illustrates a small portion of the conforming mesh generated using CISAMR for the SVE with misaligned collagen fibrils shown in Figure 7b ($V_f = 39.0\%$). A $320 \times 320 \times 160$ structured background mesh, together with one level of h -adaptive refinement along fibril and void surfaces, is utilized to create this mesh. Note that similar mesh parameters are used for all other SVEs studied in this work. The resulting conforming mesh for the current SVE has more than 24 million elements, which corresponds to ~ 28 million degrees of freedom (DOFs). Note that it would not be feasible to generate such a massive mesh sequentially due to the high computational cost and the excessive memory required for this task. Therefore, we have implemented

the parallel CISAMR algorithm introduced in Liang et al. (2019) to create this mesh using 64 processors.

4 Results and discussions

In this section, we investigate the piezoelectric response of the bone under compressive and shear loads through high-fidelity FE simulations. Eight bone SVEs with dimensions $800\text{nm} \times 800\text{nm} \times 400\text{nm}$ (4 aligned and 4 misaligned) were virtually reconstructed and converted into FE models using parallel CISAMR. The volume fraction of collagen fibrils in SVEs with aligned fibrils are $V_f = 30.8\%, 36.5\%, 41.6\%$, and 45.7% , while for SVEs with misaligned fibrils $V_f = 33.8\%, 38.2\%, 39.0\%$, and 45.4% . These volume fraction values are within the typical range found in the human bone tissue *i.e.*, $30\% < V_f < 45\%$ (Schwarcz et al. 2017). The voids volume fractions for aligned SVEs are $V_{\text{void}} = 16.6\%, 17.1\%, 16.4\%$, and 15.7% , while for SVEs with misaligned fibrils $V_{\text{void}} = 15.8\%, 16.0\%, 16.0\%$ and 15.4% . The relatively constant volume fraction of voids in these SVEs allows comparing their piezoelectric behavior only based on the volume fraction of the collagen fibrils.

Each SVE is analyzed subject to three loading conditions corresponding to those sustained by the bone during the remodeling process: Longitudinal compression (in the z direction), lateral compression (in the x direction), and shear parallel to the xy plane. These loadings are applied using displacement boundary conditions along respective faces of the SVE (*e.g.*, in the z direction along the top and bottom edges under longitudinal compression) to induce a macroscopic normal or shear strain of $\epsilon^M = 2.5 \times 10^{-6}$. To avoid rigid body motions, the displacement in one of the mesh nodes is fully constrained. Also, the initial electric potential in the domain is set to zero.

The material properties (E , ν , and D) of the collagen and mineral phases used in the FE model are given in Table 1. A matrix representation of the piezoelectric constant tensor is adopted from Denning et al. (2017), which can be expressed as

$$[d] = \begin{bmatrix} d_{111}^\psi & d_{122}^\psi & d_{133}^\psi & d_{112}^\psi & d_{113}^\psi & d_{123}^\psi \\ d_{211}^\psi & d_{222}^\psi & d_{233}^\psi & d_{212}^\psi & d_{213}^\psi & d_{223}^\psi \\ d_{311}^\psi & d_{322}^\psi & d_{333}^\psi & d_{312}^\psi & d_{313}^\psi & d_{323}^\psi \end{bmatrix}. \quad (12)$$

For collagen fibrils, components of this matrix are given by

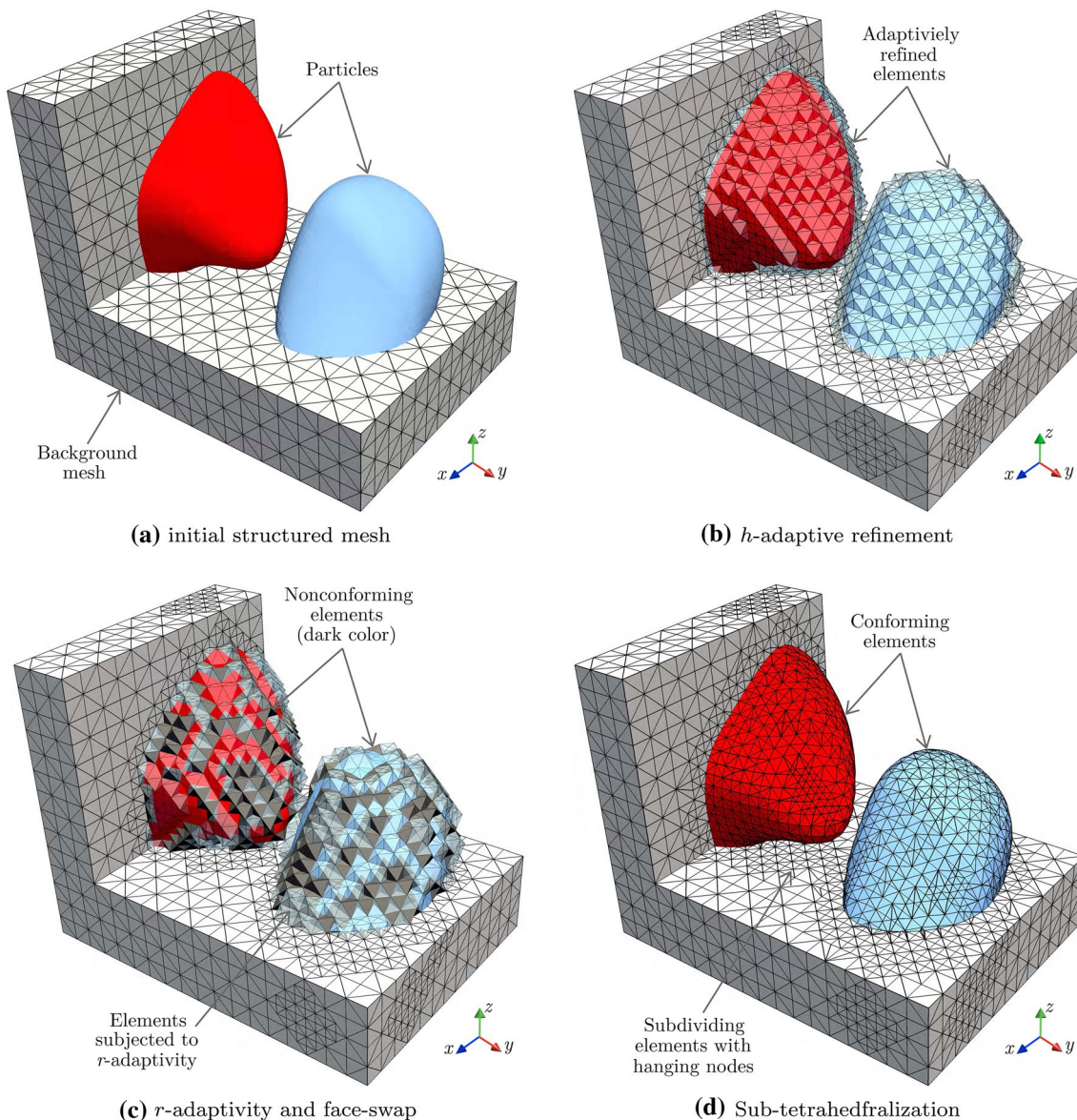


Fig. 8 Construction of a conforming mesh using CISAMR: **a** initial structured background mesh; **b** adaptively refined mesh after the SAMR phase; **c** deformed mesh after performing r -adaptivity and

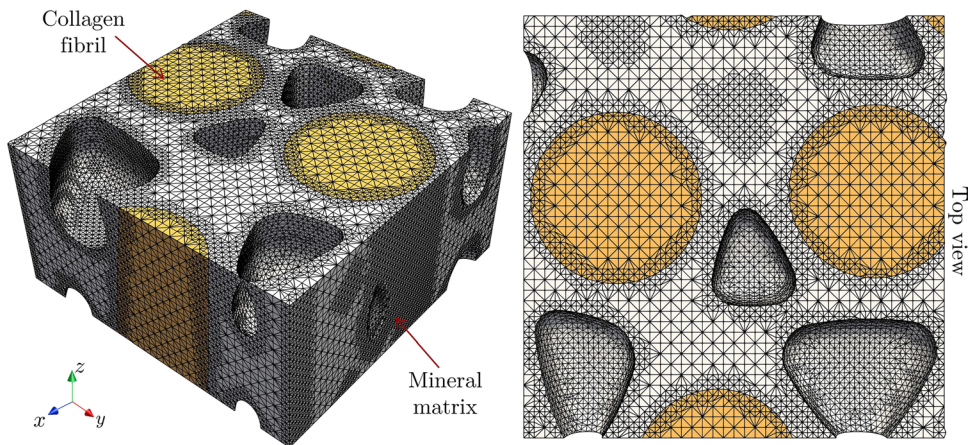
face-swap phases; **d** final conforming mesh after the completion of the sub-tetrahedralization process

$$[d] = \begin{bmatrix} 0 & 0 & 0 & -12 & 6.21 & 0 \\ 0 & 0 & 0 & 6.21 & 12 & 0 \\ -4.81 & -4.81 & 0.89 & 0 & 0 & 0 \end{bmatrix} \text{pm V}^{-1}. \quad (13)$$

Note that reducing the 27 components of third-order tensor d_{ijk}^ψ to 18 components in (12) is made possible due to symmetry features of this tensor, *e.g.*, $d_{321}^\psi = d_{312}^\psi$. This condition can easily be realized from (2), where the symmetry of the stress tensor σ_{jk} necessitates the symmetry of d_{ijk}^ψ components with similar dummy indices ($d_{ijk}^\psi = \frac{\partial q_i}{\partial \sigma_{jk}}$).

Figure 10 illustrates the FE approximation of the normal strain (ϵ_{33}) and the electric potential gradient (E_3), both in the z direction, in the SVEs previously shown in Fig. 7 subject to a longitudinal compression in the z direction. Given the large number of DOFs associated with FE models analyzed in this work (> 25 million), all simulations were conducted in parallel using 48 partitions in the FE software Abaqus, resulting in a simulation time of approximately 4 hours. As shown in Fig. 10a, although the compressive load causes an average strain of $\epsilon_{33} = -2.5 \times 10^{-6}$ in the SVE with aligned fibrils, there are multiple sites of strain

Fig. 9 Conforming mesh generated using parallel CISAMR for one of the 64 partitions of the SVE with misaligned collagen fibrils shown in Fig. 7b



concentrations that strongly correlate to the location of nearby voids. The ϵ_{33} field in the SVE with misaligned fibrils follow a similar pattern (*cf.* Figure 10c), although strain concentrations are slightly magnified in misaligned fibrils. Also, as shown in Fig. 10b and d, the variation of E_3 in both SVEs follows a similar pattern as ϵ_{33} in collagen fibrils, *i.e.*, a higher electric field is observed in regions with higher strain concentrations.

Variations of homogenized σ_{33}^M and E_3^M versus the volume fraction of collagen fibrils in all 8 SVEs (4 with aligned and 4 with misaligned fibrils) subject to a longitudinal compression are shown in Fig. 11a and b, respectively. In both types of SVE (aligned *vs.* misaligned fibrils), σ_{33}^M varies linearly with V_f , meaning only the fibrils volume fraction affect σ_{33}^M and the impact of spatial arrangement and orientation (alignment) of fibrils is negligible. On the other hand, a clear distinction is observed between $E_3^M - V_f$ responses of SVEs with aligned and misaligned fibrils. As shown in Fig. 11b, although both types of SVEs show a nearly linear increase in the homogenized electric field with an increase in V_f , for the same volume fraction, the SVEs with misaligned fibrils have between 8% and 12% higher E_3^M values.

This increase can be explained using (2), which can be rewritten in the matrix form as

$$\{q\} = [d]\{\tilde{\sigma}\} + [D]\{E\}. \quad (14)$$

Recall that in the matrix representation of the stress tensor, $\sigma_{11} \rightarrow \tilde{\sigma}_1$, $\sigma_{22} \rightarrow \tilde{\sigma}_2$, $\sigma_{33} \rightarrow \tilde{\sigma}_3$, $\sigma_{12} \rightarrow \tilde{\sigma}_4$, $\sigma_{13} \rightarrow \tilde{\sigma}_5$, and $\sigma_{23} \rightarrow \tilde{\sigma}_6$. Applying a longitudinal compression in the z direction on the nanostructure results in lateral stresses $\tilde{\sigma}_1$ and $\tilde{\sigma}_2$ in the collagen fibrils. According to the conservation of flux equation given in (2), the negative values of piezoelectric constants d_{31} and d_{32} leads to the negative term $d_{31}\tilde{\sigma}_1 + d_{32}\tilde{\sigma}_2$, which in turn reduces E_3 . Therefore, due to the smaller lateral stresses (in an average sense) developed in misaligned collagen fibrils under longitudinal compression,

corresponding SVEs yield higher values of homogenized electric field in the z direction.

The simulated normal strain in the x direction, ϵ_{11} , and the electric field in the z direction, E_3 , in two SVEs subject to a lateral compression in the x direction are illustrated in Fig. 12. Once again, the footprint of voids on sites of concentration of ϵ_{11} and E_3 in the collagen fibrils is evident in this figure. However, unlike SVEs subjected to longitudinal compression, in this case strain concentrations and consequently local electrical field variations have a negligible difference in aligned and misaligned fibrils (*cf.* Fig. 12c and d). Note that the higher strain/electric field observed in some of the fibrils is due to the size/location of their nearby voids and not the spatial orientation of fibrils. Therefore, as shown in Fig. 13, the difference between homogenized $E_3^M - V_f$ response of SVEs with aligned and misaligned fibrils is less significant in this case. On the other hand, compared to σ_{33}^M values reported for SVEs under a longitudinal compression, there is a larger discrepancy between σ_{11}^M values of SVEs with aligned and misaligned fibrils under lateral compression. In particular, a sudden jump is observable in $\sigma_{11}^M - V_f$ response of two misaligned SVEs with similar volume fractions ($V_f = 38.2\%$ and 39.0%) in Fig. 13a. This kink is attributed to the anisotropy introduced by the orientation of misaligned fibrils, meaning when more fibrils lean towards the loading direction (here, along the x -axis) the SVE shows a higher stiffness.

Further analysis of the $E_3^M - V_f$ responses of SVEs with aligned collagen fibrils subject to the lateral compression (*cf.* Fig. 13b) shows a linear response, which is similar to that of SVEs under a longitudinal compression. The key difference is the approximately one order of magnitude higher value of E_3^M associated with the former type of loading. Note that unlike SVEs subjected to longitudinal compression, in this case E_3^M is negative. The substantial difference between E_3^M values associated with lateral versus

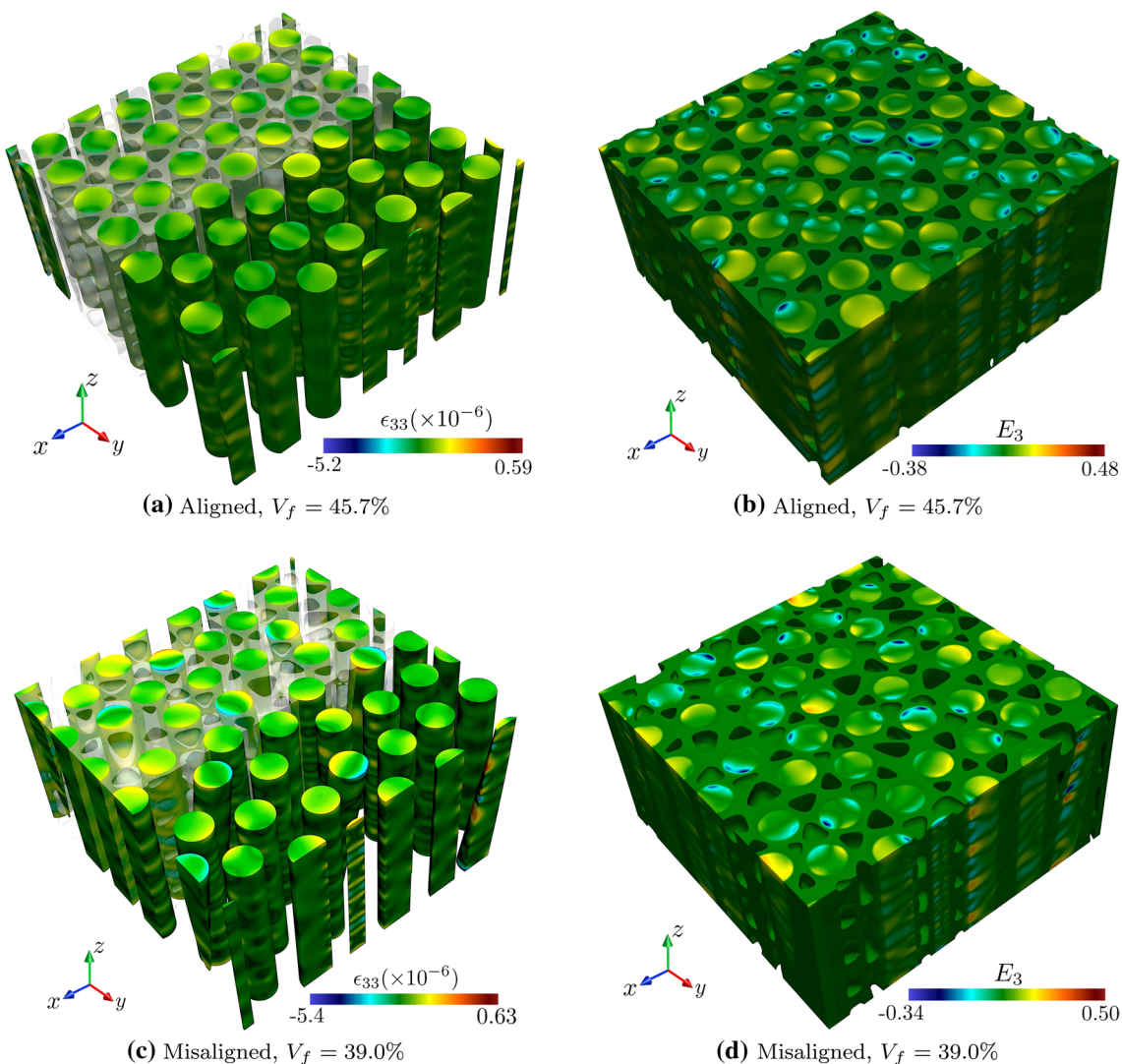


Fig. 10 Normal strain, ϵ_{33} , and electric field, E_3 [V m^{-1}], in the z direction in two SVEs with **a,b** aligned and **c,d** misaligned collagen fibrils subject to longitudinal compression

longitudinal loadings can once again be explained using (Eq. 14). Because the SVE is charge free (the flux vector $\{q\}$ is zero), the E_3 value depends on the product of piezoelectric constant tensor of collagen fibrils and the stress tensor as $d_{31}\tilde{\sigma}_1 + d_{32}\tilde{\sigma}_2 + d_{33}\tilde{\sigma}_3$. Since the components $d_{31} = d_{32} = -4.81$ are much higher than $d_{33} = 0.89$, the magnitude of this term (and thereby E_3^M) is higher under a lateral compression.

Comparing the E_3^M - V_f responses of SVEs with misaligned fibrils subject to a lateral compression in Fig. f13b with those under a longitudinal compression (*cf.* Figure 11b) shows a number of differences. Unlike the latter loading condition, for lateral compression, there is a much smaller difference ($< 4\%$) between homogenized E_3^M values associated SVEs with misaligned and aligned fibrils for the same volume fraction. Also note the oscillatory nature of the E_3^M - V_f response

of SVEs with misaligned fibrils in Fig. f13b, where E_3^M could be slightly smaller or larger than that of SVEs with aligned fibrils. Another distinct feature that stands out in this case is the sharp kink in the E_3^M - V_f response of misaligned SVEs under a lateral compression, which is compatible with the kink previously observed in their σ_{11}^M - V_f response (*cf.* Figure 13a).

We also studied the impact of SVE nanostructure on its piezoelectric response subject to a shear force applied in the transverse fibers direction. The FE approximation of the shear strain, ϵ_{13} , and the electric field in the y direction, E_2 , in the SVE with $V_f = 39.0\%$ (misaligned fibrils) are depicted in Fig. 14. Once again, the effect of voids in the mineral phase on strain concentrations in the SVE is evident in this figure. The corresponding variation of homogenized electric fields in the x and y directions, E_1^M and E_2^M , versus V_f are

Fig. 11 Variation of the homogenized **a** normal stress in the z direction, σ_{33}^M [MPa], and **b** electric field in the z direction, E_3^M [V nm^{-1}], versus the volume fraction of collagen fibrils in SVEs subject to longitudinal compression

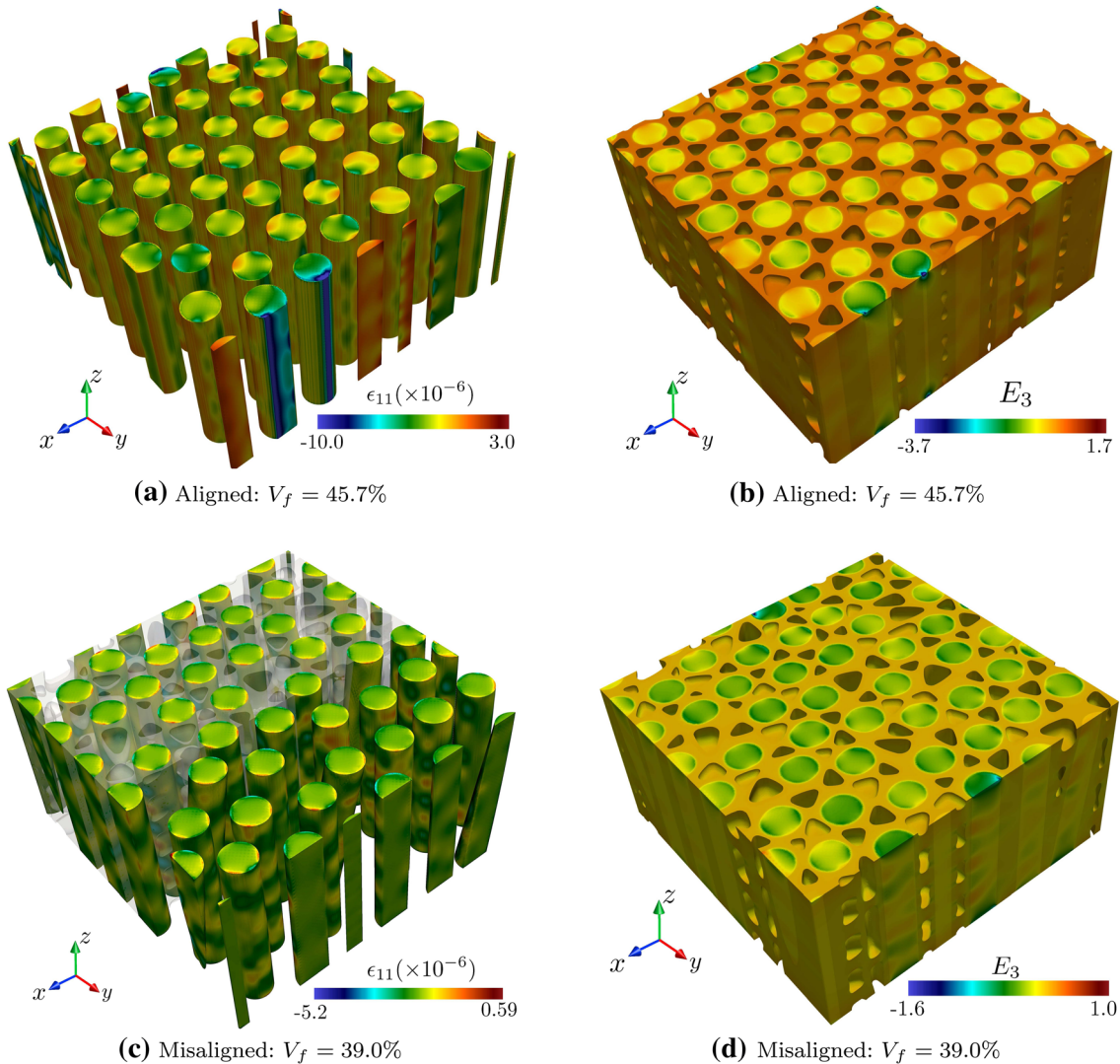
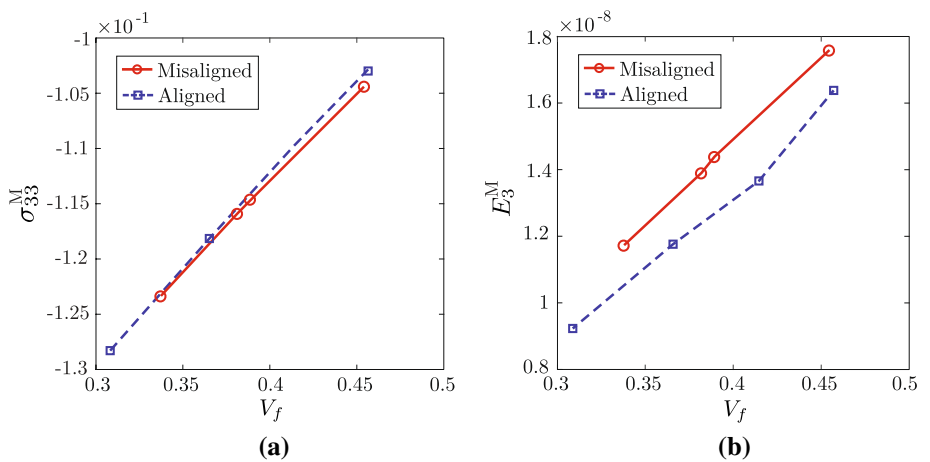


Fig. 12 Normal strain, ϵ_{11} , and electric field, E_3 [V nm^{-1}], in the z direction in two SVEs with **a,b** aligned and **c,d** misaligned collagen fibrils subject to lateral compression

Fig. 13 Variation of the homogenized **a** normal stress in the x direction, σ_{11}^M [MPa], and **b** electric field in the z direction, E_3^M [V nm^{-1}], versus the volume fraction of collagen fibrils in SVEs subject to compression in the x direction

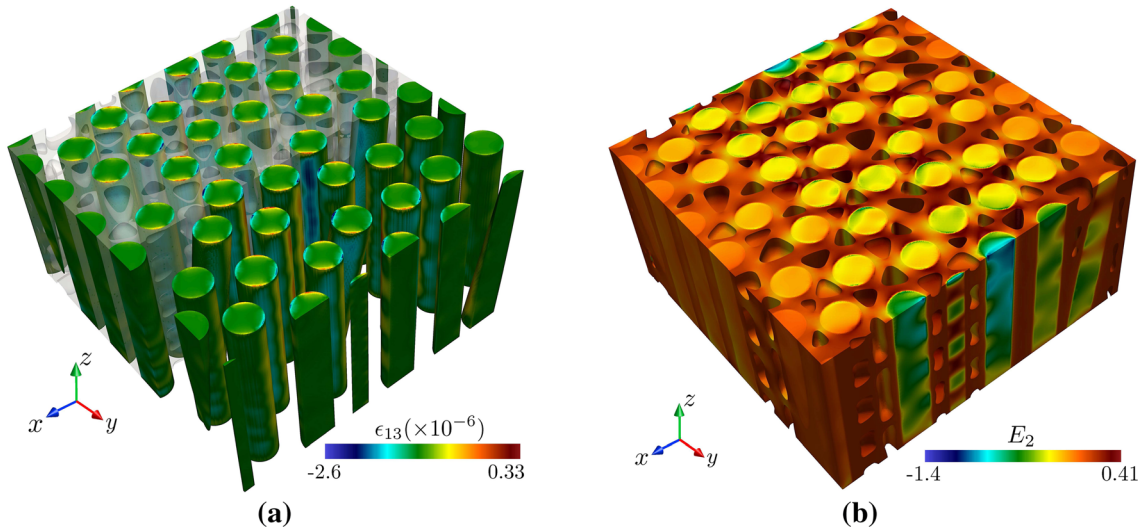
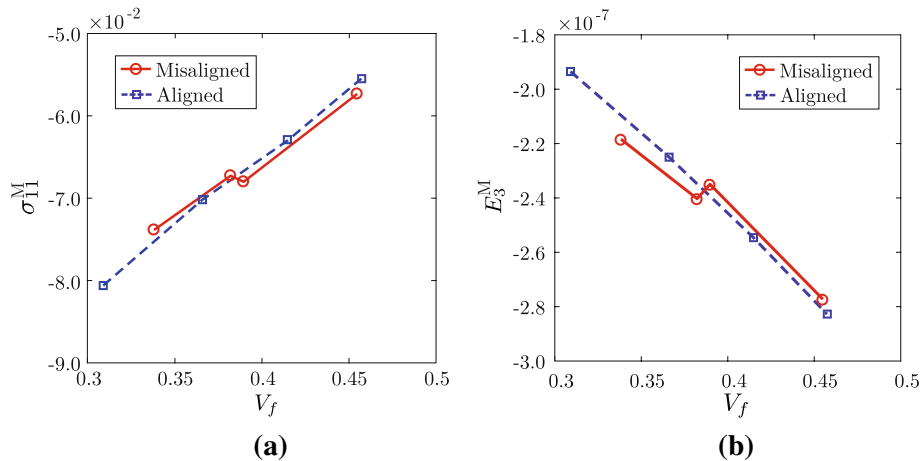


Fig. 14 **a** Shear strain, ϵ_{13} , and **b** electric field in the y direction, E_2 , and in an SVE with misaligned fibrils ($V_f = 39.0\%$) subject to shear in the transverse fibers direction

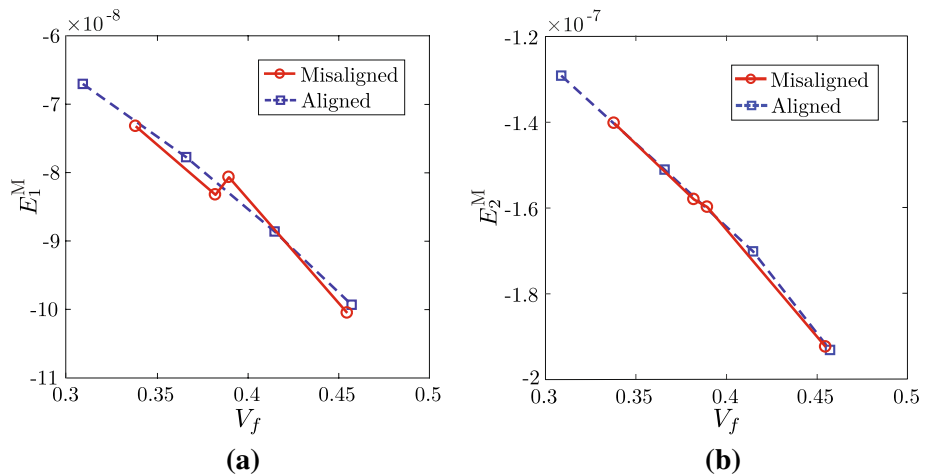
illustrated in Fig. 15. Note that the homogenized electric field in the z direction, E_3^M , has a negligible relative value in this case and thus not included in this analysis. Studying Fig. 15 shows no meaningful difference between responses of SVEs with aligned and misaligned fibrils, although more fluctuations are observed in the latter compared to the nearly linear response of the former. In particular, note the kink in the E_1^M - V_f response of misaligned SVEs (cf. Figure 15a), occurring due to the same reasons explained for the kink observed in Fig. f13b under lateral compression.

It is worth mentioning that magnitudes of E_1^M and E_2^M in SVEs subjected to a transverse shear is closer to the E_3^M obtained under a lateral compression and 7 to 10 times larger than E_3^M corresponding to a longitudinal compressive load. Moreover, for a given V_f , $E_2^M \approx 2E_1^M$, which can

be explained by comparing piezoelectric constants directly affecting these homogenized fields in (14), as $d_{25}\tilde{\sigma}_5 \approx 2d_{15}\tilde{\sigma}_5$ ($d_{25} = 12$, $d_{15} = 6.21$).

Studying the response of SVEs under lateral compression and shear leadings shows notable electric potentials are generated along the surface of collagen fibrils in the x and y directions. This surface charge is important, as it attracts charged mineral precursors onto the collagen surface for further mineralization (Ahn and Grodzinsky 2009; Niu et al. 2017), while E_3 would be beneficial for the growth of minerals along the fibril direction. It is well-known that stereochemistry of collagen polypeptides enables calcium and phosphate ions to transform nanoplates and grow along the collagen fibrils direction (z -axis). Charged residues are considered as the principal guide for the crystal growth and

Fig. 15 Variation of the homogenized electric fields in **a** x direction, E_1^M [V nm $^{-1}$], and **b** y direction, E_2^M [V nm $^{-1}$], versus the volume fraction of collagen fibrils in SVEs subject to shear in the transverse fibers direction



development (Stock 2015; Habraken et al. 2013; Silver and Landis 2011). In this manner, the additional electric field in the collagen fibrillar direction may assist the growth of crystalized minerals. Thus, mechanical stresses in various directions may provide diverse functions, such as attracting mineral clusters onto and into collagen fibrils, as well as assisting the growth of crystalized mineral inside the fibrils.

5 Conclusion

We studied the impact of the nanostructure, *i.e.*, the volume fraction and spatial orientation of collagen fibrils, on the piezoelectric response of human bone. A new virtual reconstruction algorithm was introduced to automatically generate realistic SVEs of the bone at the sub-micron scale incorporating fibril misalignment and the voids within the mineral matrix. Using a parallel non-iterative meshing algorithm named CISAMR, these SVEs were transformed into high-fidelity FE models consisting of tens of millions of elements. Eight SVEs with different fibril volume fractions, half with fully aligned and the other half with misaligned fibrils, were then reconstructed, meshed, and their piezoelectric responses were simulated under three loading conditions: longitudinal compression, lateral compression, and shear in the transverse fibrils directions. Key takeaways from analyzing the simulation results are summarized below:

1. For all loading conditions, the nonzero component of homogenized electric field in SVEs with aligned fibrils (*e.g.*, E_3^M under lateral compression) linearly varies with respect to the volume fraction of fibrils, V_f .
2. The magnitude of E_3^M under longitudinal compression is approximately one order of magnitude smaller than E_3^M under lateral compression and E_1^M/E_2^M under transverse shear.

3. While under longitudinal compression, the homogenized electric field E_3^M in SVEs with misaligned fibrils is notably larger than the response of SVEs with aligned fibrils, under the other two loading conditions, the difference between the homogenized response of aligned and misaligned SVEs is negligible.
4. The electric fields generated by lateral compression and shear strains induce electric potentials on a collagen surface, which can increase the zeta-potentials of collagen fibrils and help attracting charged mineral precursors onto collagen surface for mineralization.

Acknowledgements This work has been supported by a seed grant from the Ohio State University's Institute for Materials Research (IMR). The corresponding author also acknowledges partial support through Air Force Office of Scientific Research (AFOSR) under grant number FA9550-17-1-0350.

Declarations

Conflicts of interest The authors declare that they have no conflict of interest.

References

Ahn AC, Grodzinsky AJ (2009) Relevance of collagen piezoelectricity to "wolff's law": a critical review. *Med Eng Phys* 31(7):733–741

Bar-On B, Wagner HD (2011) Mechanical model for staggered biostructure. *J Mech Phys Solids* 59(9):1685–1701

Bassett CA (1965) Electrical effects in bone. *Sci Am* 213(4):18–25

Denning D, Kilpatrick JI, Fukada E, Zhang N, Habelitz S, Fertala A, Gilchrist MD, Zhang Y, Tofail Syed AM, Rodriguez BJ (2017) Piezoelectric tensor of collagen fibrils determined at the nanoscale. *ACS Biomater Sci Eng* 3(6):929–935

Du Q, Faber V, Gunzburger M (1999) Centroidal voronoi tessellations: applications and algorithms. *SIAM Rev* 41(4):637–676

Fratzl P, Weinkamer R (2007) Nature's hierarchical materials. *Prog Mater Sci* 52(8):1263–1334

Fukada E, Yasuda I (1964) Piezoelectric effects in collagen. *Japan J Appl Phys* 3(2):117

Genin GM, Kent A, Birman V, Wopenka B, Pasteris JD, Marquez PJ, Thomopoulos S (2009) Functional grading of mineral and collagen in the attachment of tendon to bone. *Biophys J* 97(4):976–985

Gjelsvik A (1973) Bone remodeling and piezoelectricity-i. *J Biomech* 6(1):69–77

Habraken WJ, Tao J, Brylka LJ, Friedrich H, Bertinetti L, Schenk AS, Verch A, Dmitrovic V, Bomans PH, Frederik PM et al (2013) Ion-association complexes unite classical and non-classical theories for the biomimetic nucleation of calcium phosphate. *Nat Commun* 4(1):1–12

Hamed E, Lee Y, Jasiuk I (2010) Multiscale modeling of elastic properties of cortical bone. *Acta Mechanica* 213(1–2):131–154

Hang F, Barber AH (2011) Nano-mechanical properties of individual mineralized collagen fibrils from bone tissue. *J Royal Soc Interface* 8(57):500–505

Hill R (1985) On the micro-to-macro transition in constitutive analyses of elastoplastic response at finite strain. In *Mathematical Proceedings of the Cambridge Philosophical Society*, volume 98, pages 579–590. Cambridge Univ Press

Ji B, Gao H (2004) Mechanical properties of nanostructure of biological materials. *J Mech Phys Solids* 52(9):1963–1990

Jong De M, Chen W, Geerlings H, Asta M, Persson KA (2015) A database to enable discovery and design of piezoelectric materials. *Sci Data* 2(1):1–13

Jäger I, Fratzl P (2000) Mineralized collagen fibrils: a mechanical model with a staggered arrangement of mineral particles. *Biophys J* 79(4):1737–1746

Kalinin SV, Rodriguez BJ, Shin J, Jesse S, Grichko V, Thundat T, Baddorf AP, Gruverman A (2006) Bioelectromechanical imaging by scanning probe microscopy: Galvani's experiment at the nanoscale. *Ultramicroscopy* 106(4–5):334–340

Kaygili O, Dorozhkin SV, Ates T, Al-Ghamdi AA, Yakuphanoglu F (2014) Dielectric properties of Fe doped hydroxyapatite prepared by sol-gel method. *Ceram Int* 40(7):9395–9402

Landis WJ, Hodgens KJ, Arena J, Song MJ, McEwen BF (1996) Structural relations between collagen and mineral in bone as determined by high voltage electron microscopic tomography. *Microsc Res Tech* 33(2):192–202

Launey ME, Buehler MJ, Ritchie RO (2010) On the mechanistic origins of toughness in bone. *Ann Rev Mater Res* 40:25–53

Liang B, Nagarajan A, Soghrati S (2019) Scalable parallel implementation of cisamr: a non-iterative mesh generation algorithm. *Comput Mech* 64(1):173–195

Madarash-Hill C, Hill JB (2004) Enhancing access to IEEE conference proceedings: a case study in the application of IEEE Xplore full text and table of contents enhancements. *Science & Technology Libraries* 24(3–4):389–399

Marino AA, Becker RO, Soderholm SC (1971) Origin of the piezoelectric effect in bone. *Calcif Tissue Res* 8(1):177–180

Martínez-Ayuso G, Friswell MI, Adhikari S, Khodaparast HH, Berger H (2017) Homogenization of porous piezoelectric materials. *Int J Solids Struct* 113:218–229

Martínez-Reina J, Domínguez J, García-Aznar JM (2011) Effect of porosity and mineral content on the elastic constants of cortical bone: a multiscale approach. *Biomech Model Mechanobiol* 10(3):309–322

McNally E, Nan F, Botton GA, Schwarcz HP (2013) Scanning transmission electron microscopic tomography of cortical bone using z-contrast imaging. *Micron* 49:46–53

McNally EA, Schwarcz HP, Botton GA, Arsenault AL (2012) A model for the ultrastructure of bone based on electron microscopy of ion-milled sections. *PLOS one* 7(1):e29258

Minary-Jolandan M, Yu MF (2009) Nanoscale characterization of isolated individual type I collagen fibrils: polarization and piezoelectricity. *Nanotechnology* 20(8):085706

Nagarajan A, Soghrati S (2018) Conforming to interface structured adaptive mesh refinement: 3D algorithm and implementation. *Computational Mechanics*, pages 1–26

Nikolov S, Raabe D (2008) Hierarchical modeling of the elastic properties of bone at submicron scales: the role of extrafibrillar mineralization. *Biophys J* 94(11):4220–4232

Niu L, Jee SE, Jiao K, Tonggu L, Li M, Wang L, Yang Y, Bian J, Breschi L, Jang SS et al (2017) Collagen intrafibrillar mineralization as a result of the balance between osmotic equilibrium and electroneutrality. *Nat Mater* 16(3):370–378

Norman TL, Vashishth D, Burr DB (1995) Fracture toughness of human bone under tension. *J Biomech* 28(3):309–320

Pieg L, Tiller W (2012) The NURBS book. Springer, Berlin

Reilly DT, Burstein AH, Frankel VH (1974) The elastic modulus for bone. *J Biomech* 7(3):271–275

Reznikov N, Bilton M, Lari L, Stevens MM, Kröger R (2018) Fractal-like hierarchical organization of bone begins at the nanoscale. *Science* 360(6388):ea02189

Reznikov N, Shahar R, Weiner S (2014) Bone hierarchical structure in three dimensions. *Acta Biomaterialia* 10(9):3815–3826

Rho JY, Kuhn-Spearing L, Ziopoulos P (1998) Mechanical properties and the hierarchical structure of bone. *Med Eng Phys* 20(2):92–102

Ritchie RO, Buehler MJ, Hansma P (2009) Plasticity and toughness in bone. American Institute of Physics

Sabet FA, Raeisi Najafi A, Hamed E, Jasiuk I (2016) Modelling of bone fracture and strength at different length scales a review. *Interface Focus* 6(1):20150055

Sanchez PF (2013) Microstructural model of the collagen fibril using finite element method

Santulli C (2015) Bio-inspired fiber composites. In *Biomimetic technologies*. Elsevier, pp 33–51

Schwarz HP, Abueidda D, Jasiuk I (2017) The ultrastructure of bone and its relevance to mechanical properties. *Front Phys* 5:39

Shen ZL, Dodge MR, Kahn H, Ballarini R, Eppell SJ (2008) Stress-strain experiments on individual collagen fibrils. *Biophys J* 95(8):3956–3963

Silver FH, Landis WJ (2011) Deposition of apatite in collagenous extracellular matrices: identification of possible nucleation sites on type I collagen. *Conn Tis Res* 52(3):242–252

Soghrati S, Nagarajan A, Liang B (2017) Conforming to interface structured adaptive mesh refinement: new technique for the automated modeling of materials with complex microstructures. *Finite Elem Anal Des* 125:24–40

Stock SR (2015) The mineral-collagen interface in bone. *Calcif Tissue Int* 97(3):262–280

Taylor D, Hazenberg JG, Lee TC (2007) Living with cracks: damage and repair in human bone. *Nat Mater* 6(4):263–268

Tofail S, Zhang Y, Gandhi AA (2011) Piezoelectricity of bone from a new perspective. In *2011-14th International Symposium on Electrets*, pages 91–92. IEEE

Tomaselli VP, Shamos MH (1973) Electrical properties of hydrated collagen I dielectric properties. *Biopolym Org Res Biomole* 12(2):353–366

Tong W, Glimcher MJ, Katz JL, Kuhn L, Eppell SJ (2003) Size and shape of mineralites in young bovine bone measured by atomic force microscopy. *Calcif Tissue Int* 72(5):592–598

Vercher A, Giner E, Arango C, Tarancón JE, Fuenmayor FJ (2014) Homogenized stiffness matrices for mineralized collagen fibrils and lamellar bone using unit cell finite element models. *Biomech Model Mechanobiol* 13(2):437–449

Wang Y, Ural A (2018) Mineralized collagen fibril network spatial arrangement influences cortical bone fracture behavior. *J Biomech* 66:70–77

Wang Z, Vashishth D, Picu RC (2018) Bone toughening through stress-induced non-collagenous protein denaturation. *Biomech Model Mechanobiol* 17(4):1093–1106

Wegst UGK, Bai H, Saiz E, Tomsia AP, Ritchie RO (2015) Bioinspired structural materials. *Nat Mater* 14(1):23

Weiner S, Arad T, Traub W (1991) Crystal organization in rat bone lamellae. *FEBS Lett* 285(1):49–54

Weiner S, Traub W (1992) Bone structure: from angstroms to microns. *The FASEB J* 6(3):879–885

Weiner S, Wagner HD (1998) The material bone: structure-mechanical function relations. *Ann Rev Mater Sci* 28(1):271–298

Wenger Marco PE, Bozec L, Horton MA, Mesquida P (2007) Mechanical properties of collagen fibrils. *Biophys J* 93(4):1255–1263

Yang L (2008) Mechanical properties of collagen fibrils and elastic fibers explored by afm. University of Twente, Enschede

Yang L, Van der Werf KO, Fitié Carel FC, Bennink ML, Dijkstra PJ, Feijen J (2008) Mechanical properties of native and cross-linked type I collagen fibrils. *Biophys J* 94(6):2204–2211

Yang G, Xiao L, Lamboni L, Wiley J (2018) Bioinspired materials science and engineering. Wiley, Hoboken

Yuan F, Stock SR, Haeffner DR, Almer JD, Dunand DC, Brinson LC (2011) A new model to simulate the elastic properties of mineralized collagen fibril. *Biomech Model Mechanobiol* 10(2):147–160

Zhang ZQ, Liu B, Huang Y, Hwang KC, Gao H (2010) Mechanical properties of unidirectional nanocomposites with non-uniformly or randomly staggered platelet distribution. *J Mech Phys Solids* 58(10):1646–1660

Publisher's Note Springer Nature remains neutral with regard to jurisdictional claims in published maps and institutional affiliations.